Phase Matching for Multimode Four-Wave Mixing in Few-Mode Fibers and Nano-Rib Waveguides

Tasnad Kernetzky and Norbert Hanik

***Abstract*—We compare phase matching for four-wave mixing using one, two, three, and four waveguide modes. For the comparison, we use numerical optimizations and an estimate of the generated idler power. We present results for few-mode fibers and nano-rib waveguides and show that for both waveguide types, four-wave mixing bandwidths and idler powers are best for one- and two-mode operation and that four-mode four-wave mixing is not feasible at all. Some nano-rib waveguides support three-mode four-wave mixing, albeit with much reduced bandwidth and reduced idler power.**

***Index Terms*—nonlinear optics, phase matching, multimode waveguide, four-wave mixing, few-mode fiber, SOI nano-rib waveguide**

I. Introduction

Four-wave mixing (FWM) is usually regarded as a detrimental effect for optical communications over long fiber links. Although silica has a relatively low nonlinearity coefficient γ, the long propagation distance of up to thousands of kilometers leads to non-negligible nonlinear distortions. There exist different approaches for mitigating these effects, one of which is optical phase conjugation (OPC). There, FWM is intentionally used in a lumped device in the middle of the optical link to cancel linear and nonlinear phase distortions caused by chromatic dispersion and fiber nonlinearity. A second use case for FWM utilizes the so-called Bragg scattering (BS) process to all-optically shift the frequency of transmission channels or even bands.

To process an optical signal by means of FWM, it is sent into a cubic nonlinear medium, together with two strong pumps. If laser frequencies, waveguide geometry and choice of modes are well-selected, the nonlinearity will generate an idler wave with the desired properties (conjugated phase and/or shifted frequency). Typically, two configurations are used for waveguide modes and laser frequencies: one-mode four-wave mixing (1-FWM) and two-mode four-wave mixing (2-FWM). In 1-FWM, all lasers (signal and pumps) are launched into the same mode, and the idler will be generated in the same mode as well. For phase matching (PM), frequencies need to be close to a zero dispersion region of the waveguide (e.g., [1]). In 2-FWM, the signal and one pump are launched into one mode, while the other pump is launched into another mode where also the idler will be generated (e.g., [2]). In three-mode four-wave mixing (3-FWM), signal, pumps and idler propagate in exactly three different modes (two modes with one wave, one mode with two waves). Finally, in four-mode four-wave mixing (4-FWM), all waves propagate in four different modes. While there exist analytical expressions for PM in 1-FWM and 2-FWM, numerical optimizations are necessary for 3-FWM and 4-FWM.

The authors are with Technical University of Munich.
E-mails: tasnad@tum.de and norbert.hanik@tum.de.
This work was supported by DFG project HA 6010/6-1.

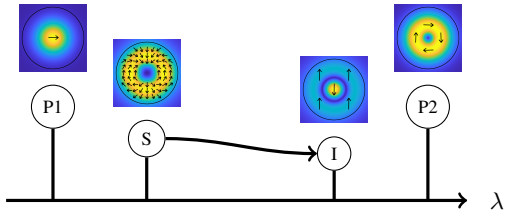

Fig. 1. Example of an OPC 4-FWM process. Note that this figure is merely an example and modes are not selected according to any specific condition.

In this work, we compare FWM bandwidths (by a metric B_{FWM}, see Definition 1) and nonlinearity parameters γ, for the cases of 1-FWM, 2-FWM, 3-FWM and 4-FWM. We consider graded index depressed cladding few-mode fibers (FMFs) and nano-rib (NR) silicon waveguides, both with different geometries. We chose these two types of waveguides, since they are widely used for all-optical signal processing (e.g. [2], [3]).

In [4], [5], we presented a 2-FWM system experiment which demonstrates all-optical conversion of three channels from C- to O-band. The extension of all-optical signal processing to more than two modes in future space-division multiplex networks could potentially be beneficial. Hence, we explore its feasibility in this paper.

II. Four-Wave Mixing and Phase Matching

The principle of multimode FWM is sketched in Fig. 1. It shows an example of a four-mode OPC operation (each wave propagates in a different mode) with pumps P_1 and P_2, signal S and idler I.

Photon energy ($\hbar\omega$) and photon momentum ($\hbar\beta$) conservation for the BS and OPC processes lead to

$$\text{BS}: \omega_{\mathrm{I}} = \omega_{\mathrm{P}_1} + \omega_{\mathrm{S}} - \omega_{\mathrm{P}_2} \tag{1}$$

$$\Delta\beta = \beta^{\mathrm{A}}(\omega_{\mathrm{P}_1}) + \beta^{\mathrm{B}}(\omega_{\mathrm{S}}) - \beta^{\mathrm{C}}(\omega_{\mathrm{P}_2}) - \beta^{\mathrm{D}}(\omega_{\mathrm{I}}) \tag{2}$$

$$\text{OPC}: \omega_{\mathrm{I}} = \omega_{\mathrm{P}_1} - \omega_{\mathrm{S}} + \omega_{\mathrm{P}_2} \tag{3}$$

$$\Delta\beta = \beta^{\mathrm{A}}(\omega_{\mathrm{P}_1}) - \beta^{\mathrm{B}}(\omega_{\mathrm{S}}) + \beta^{\mathrm{C}}(\omega_{\mathrm{P}_2}) - \beta^{\mathrm{D}}(\omega_{\mathrm{I}}), \tag{4}$$

where A, B, C and D denote different modes and, e.g., β^{A} is the propagation constant of mode A. Firstly, energy conservation dictates the resulting idler frequency as a function of the input laser frequencies (Eqs. (1) and (3)). Secondly,

the efficiency of FWM depends on how well the momentum conservation equation is fulfilled, which is measured by the residual phase mismatch $\Delta\beta$ (Eqs. (2) and (4)). For increasing values of phase mismatch, the coherent buildup of the idler turns into an oscillation with decreasing period. Minimizing phase mismatch is the well-known process of *phase matching* and our approach is explained in [6] in more detail. Since modes have different propagation constants and waveguide geometry affects modes, both factors play important roles in PM.

The conclusions we derive in this article are the same for BS and OPC. Therefore, we only show results for BS and mention small differences to OPC briefly in the text.

A useful and intuitive PM approach for 1-FWM and 2-FWM was given in [2]. The group delay (see Eq. (9)) of signal and pump in one mode at their average frequency, needs to match the group delay in the other mode at the average frequency of idler and the other pump, e.g.,

$$\tau_g^{\mathrm{A}}\left(\frac{\omega_{\mathrm{P}_1}+\omega_{\mathrm{S}}}{2}\right)=\tau_g^{\mathrm{A}}\left(\frac{\omega_{\mathrm{P}_2}+\omega_{\mathrm{I}}}{2}\right)\quad\text{(1-FWM)}\qquad(5)$$

$$\tau_g^{\mathrm{A}}\left(\frac{\omega_{\mathrm{P}_1}+\omega_{\mathrm{S}}}{2}\right)=\tau_g^{\mathrm{B}}\left(\frac{\omega_{\mathrm{P}_2}+\omega_{\mathrm{I}}}{2}\right)\quad\text{(2-FWM).}\qquad(6)$$

This approach is not applicable in more-than-two-mode FWM, as for instance in the example in Fig. 1. In the general case, numerical optimizations of Eqs. (1) and (2) need to be performed to find the optima.

Since we are interested in broadband operation, we use the FWM bandwidth as metric of quality.

Definition 1. The FWM bandwidth B_{FWM} is the frequency range the signal can be moved, while the estimate of idler power does not drop by more than 3 dB from its peak value, and without changing any other parameter (waveguide dimensions, pump frequencies, mode assignments).

The propagation constant in a mode A can be expanded into its Taylor series

$$\beta^{\mathrm{A}}(\omega)=\beta_0^{\mathrm{A}}+\beta_1^{\mathrm{A}}\Delta\omega+\frac{1}{2}\beta_2^{\mathrm{A}}\Delta\omega^2+\ldots,\qquad(7)$$

$$\beta_n^{\mathrm{A}}=\left.\frac{\mathrm{d}^n\,\beta^{\mathrm{A}}(\omega)}{\mathrm{d}\omega^n}\right|_{\omega=\omega_0},\quad\Delta\omega=\omega-\omega_0\qquad(8)$$

around a center frequency ω_0. The β_0 coefficients are usually subject to fluctuations along fiber waveguides. Therefore, it is customary in 2-FWM to choose the modes such that the β_0s are canceled in Eq. (2) (see, e.g., [2]) in order to ensure disturbance-free FWM. However, it requires further studies to determine if this assumption also holds for short NR waveguides with propagation distances in the range of centimeters. In 1-FWM, the β_0s cancel automatically and in 2-FWM they can be canceled by proper mode selection. However, there is no way to select modes in 3-FWM and 4-FWM to cancel them. Thus, we ignore this limitation in the current work and allow all mode combinations. This way, we ensure a fair comparison between FWM with one to four modes.

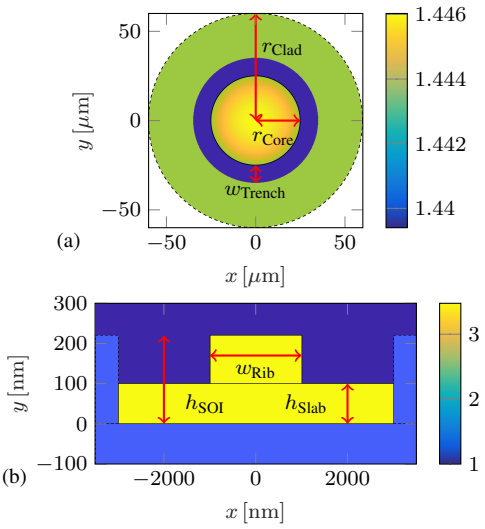

Fig. 2. Refractive index geometries. (a) FMFs with core radius, cladding radius and trench width. (b) NR waveguides with slab height, SOI height and rib width.

TABLE I
GEOMETRY VALUES CONSIDERED FOR OPTIMIZATIONS.

Parameter	Values	Number of Values
Few-Mode Fiber		
r_{Core}	6–40 µm	18
w_{Trench}	$\{0, 0.25, 0.5, 1, 2, 4, 8\}$ µm	7
r_{Clad}	$r_{\mathrm{Core}} + w_{\mathrm{Trench}} + 10$ µm	-
Δ	0.1383 %	1
Nano-Rib Waveguide		
w_{Rib}	1000–3000 nm	20
h_{Slab}	70–180 nm	12
h_{SOI}	220 nm	1

III. Geometry, Modes and Dispersion Properties of Few-Mode Fibers and Nano-Rib Waveguides

In this section, we present refractive index profiles, mode fields, and group delay curves of both, optical fibers and NR silicon waveguides. Figure 2(a) shows the FMF geometry with core radius r_{Core}, cladding radius r_{Clad} and trench width w_{Trench}. We use graded index fibers with a depressed cladding, c.f. [7]. Note that the refractive index contrast is very low, which is typical for optical fibers. The index profile has

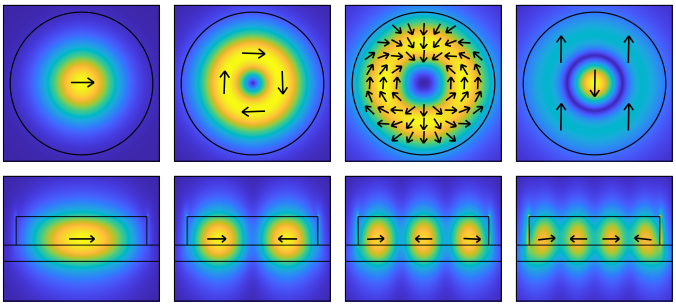

Fig. 3. Transversal electrical field distributions (magnitudes and polarization directions) of some FMF and NR waveguide modes.
FMF modes in the upper row: HE_{11e}, TE_{01}, EH_{11o} and HE_{12o}.
NR modes in the lower row: TE_0, TE_1, TE_2 and TE_3.

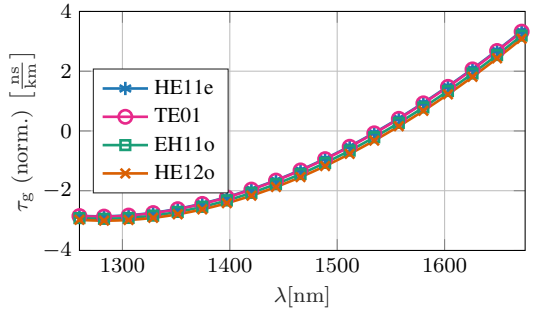

Fig. 4. Relative normalized group delay of modes in a FMF with $r_{\text{Core}} = 22\,\mu\text{m}$, $w_{\text{Trench}} = 0\,\mu\text{m}$ and $r_{\text{Clad}} = 32\,\mu\text{m}$.

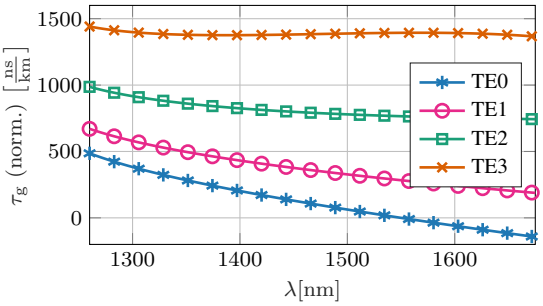

Fig. 5. Relative normalized group delay of modes in a NR waveguide with $w_{\text{Rib}} = 1947\,\text{nm}$ and $h_{\text{Slab}} = 80\,\text{nm}$.

a grading exponent of 2.0 and an ellipticity of 1.0 (i.e., perfectly round). Similarly, Fig. 2(b) shows the NR waveguide geometry with rib width w_{Rib}, slab height h_{Slab}, and silicon on insulator height h_{SOI}. The waveguide consists of a crystalline silicon core surrounded by silica, which results in a very high refractive index contrast. Table I lists the geometry values we used for optimizations.

We use a full vectorial finite difference method mode solver based on [8] to compute waveguide modes and propagation constants, from which we can derive normalized group delay and chromatic dispersion curves

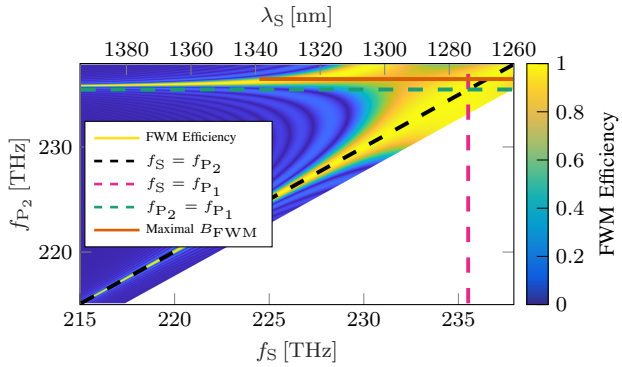

Fig. 6. Normalized FWM efficiency for a fiber with $r_{\text{Core}} = 22\,\mu\text{m}$, $w_{\text{Trench}} = 0\,\mu\text{m}$ and $r_{\text{Clad}} = 32\,\mu\text{m}$. Here, S and P_2 propagate in HE_{11e} and P_1 and I in HE_{21e}, and pump 1 is fixed at $f_{P_1} = 235.55\,\text{THz}$ (1272.7 nm). For combinations of f_S and f_{P_2} in white areas, the idler frequency f_I lies outside of the simulated frequency range (O- to U-band).

$$\tau_g^{\text{A}}(\lambda) = \frac{\mathrm{d}\beta^{\text{A}}}{\mathrm{d}\omega}\,, \qquad D^{\text{A}}(\lambda) = \frac{\mathrm{d}\tau_g^{\text{A}}}{\mathrm{d}\lambda}\,. \tag{9}$$

The normalized group delay τ_g (also called inverse group velocity) is the time per distance a signal accumulates while propagating in a waveguide. It is common to present relative values, which simply means that all curves are shifted by a constant offset – such that the slowest mode has value zero at some arbitrary wavelength (typically 1550 nm). To improve simulation accuracy, we don't fix the cladding radius to one value, but let it vary with the core radius. This way, more points of the mode solver's discretization grid are available for computing the fields in the core. We found that 10 µm outside of the core, the fields have decayed enough to be negligible. Figure 3 shows the four lowest-order (largest β) computed vectorial mode fields for both types of waveguides. Since fiber modes appear in groups with (almost) identical propagation constants (e.g., $\{HE_{11e}, HE_{11o}\}$ or $\{TE_{01}, TM_{01}, HE_{21e}, HE_{21o}\}$), we show one mode of the four lowest order *mode groups* instead. While the fiber modes have both transversal components, the nano-rib modes are approximately linearly polarized. Note that the axes have different scalings.

The group delays for one exemplary FMF and NR waveguide are shown in Figs. 4 and 5, respectively. Note that the group delays of the two waveguide types differ by orders of magnitude and also in shape (especially the weakly guided TE_3 mode).

Our waveguide optimization relies on the FWM efficiency

$$\eta_{\text{FWM}}(\Delta\beta) = \frac{1 - \exp\left(-(\alpha + j\Delta\beta)L\right)}{(\alpha + j\Delta\beta)L} \tag{10}$$

with waveguide length L and attenuation α. It was first derived in [1] and extended to FMFs in [9], by using Eq. (17) from [10]. A very similar idea is used, e.g., in [11] to assess FWM efficiency in silicon rib waveguides. Note that this is an approximative equation for a best-case analysis and we highlight some drawbacks in Section VI.

We always used $L = 2\,\text{cm}$ and $\alpha = 1\,\text{dB/cm}$ for NR waveguides and $L = 10\,\text{m}$ (see Section IV why) and $\alpha = 0.226\,\text{dB/km}$ for fibers. We always jointly optimize laser wavelengths (signal, pumps and idler) and the choice of modes, with the goal of maximal B_{FWM}.

Figure 6 shows an example of the normalized FWM efficiency $|\eta_{\text{FWM}}| \,/\, \max(|\eta_{\text{FWM}}|)$ for a FMF with $r_{\text{Core}} = 22\,\mu\text{m}$, $w_{\text{Trench}} = 0\,\mu\text{m}$ and $r_{\text{Clad}} = 32\,\mu\text{m}$. The FWM efficiency is shown as a function of pump 2 and signal frequency and all other parameters were optimized for maximal FWM bandwidth B_{FWM} in a 2-FWM operation mode (it was enforced that two modes are used with two lasers in each). The optimal values found by the optimization are S and P_2 in HE_{11e} and P_1 and I in HE_{21e}, and pump 1 fixed at $f_{P_1} = 235.55\,\text{THz}$ (or $\lambda_{P_1} = 1272.7\,\text{nm}$), leading to the presented plot and the marked B_{FWM}. It is achieved for $f_{P_2} = 236.6\,\text{THz}$ (or $\lambda_{P_2} = 1267.1\,\text{nm}$). For this choice, PM is retained for signal frequencies between 224.93–237.93 THz (1260.0–1332.8 nm). The dashed lines mark where two lasers have the same frequency and hence FWM is degenerate. To avoid

degenerate FWM, we remove configurations from the search space where signal or idler are closer to a pump than 250 GHz (roughly 2 nm). Separating the idler from pumps is strictly necessary, since waveguide imperfections always couple the strong pumps to the idler's mode as well. Thus, it is impossible to separate the idler at the end of the waveguide. Enforcing a separation between the two pumps is not strictly necessary, but in cases where they are not, the BS idler has the same frequency as the input signal (see Eq. (1)), which, of course, disables wavelength conversion. Allowing the signal to have one of the pump's frequency has a similar effect: the OPC idler is generated at the other pump's frequency (see Eq. (3)) and can't be separated any more. For further optimization results for NR waveguides, we refer to [6].

For the results in this feasibility study, we allow all lasers to be in the O-, E-, S-, C-, L or U-bands (1260–1675 nm or 179–238 THz) without any limitation and don't restrict FWM to *useful* configurations (e.g., wavelength conversion from C- to O-band, etc.) – in contrast to [6].

IV. FWM Bandwidth Optimization Results

Repeating the search for highest FWM bandwidth like in Fig. 6 for different waveguides (we used the parameters listed in Table I), allows to compare waveguide geometries. We performed separate waveguide parameter optimizations for 1-, 2-, 3- and 4-FWM. Figure 7 shows the best achievable FWM bandwidth B_{FWM} for FMF and NR waveguides. The left subfigures (a) to (c) show results for FMFs and subfigures (d) to (f) for NR waveguides. The first row shows 1-FWM, the second row 2-FWM and the third row 3-FWM.

Both waveguides have negligible FWM bandwidths for 4-FWM. Therefore, we ignore 4-FWM in the rest of this paper with the conclusion that it is not feasible.

The optimizations for FMFs were performed with only 10 m fiber length to be able to cope with the large searched bandwidth (from O- to U-band). With the reduced length, the PM bandwidth becomes larger and is better suited for numerical optimizations. In reality, the length needs to be in the range of several hundred meters up to some kilometers to build up sufficient idler powers. This means that FWM bandwidths of FMFs are much lower in reality (see, e.g., [9] and note that length reduces bandwidth in Eq. (10)). Our results for FMFs are therefore not comparable to our results for NR waveguides. This is not a problem, however, since our goal is to compare FWM with different numbers of modes, among the *same type* of waveguides.

From Fig. 7 (a) to (c), one can conclude that FWM with one, two and three modes gives roughly the same maximal FWM bandwidth in FMFs. However, the higher the number of modes, the more the optima are concentrated towards larger core radii. To understand the reason, compare the fiber with $r_{\mathrm{Core}} = 22\,\mu\mathrm{m}$ in Fig. 4 with a second fiber with $r_{\mathrm{Core}} = 40\,\mu\mathrm{m}$ in Fig. 8. Due to the large core, all the considered mode groups have very similar group delays and the process effectively becomes 1-FWM for any number of used modes.

The two best waveguides in Fig. 7 (a) have broad zero dispersion regions of one mode in the considered frequency range, which leads to high FWM bandwidths (see Eq. (5)).

For NR waveguides, comparing Fig. 7 (d) to (f) reveals that increasing the number of modes decreases FWM bandwidths. Here, larger cores also lead to approaching group delay curves (similar to Fig. 4 vs. Fig. 8), but the difference stays much larger and the process does not effectively become 1-FWM for the geometries simulated here. The difference in group delay curve shapes and magnitudes in Figs. 4 and 5 also indicates that NR waveguides behave differently. By comparing the plots in Fig. 7, it is clear that FWM in NR waveguides is more sensitive to geometry variations than in FMFs. The ultra high bandwidths (more than 10 times the C-band) in Fig. 7(d) are also based on low dispersion regions, see the TE_3 mode in Fig. 5.

The bandwidths for OPC are very similar to Fig. 7, we list the maxima: (a): $5\mathrm{B_C}$, (b): $1.8\mathrm{B_C}$, (c): $1.8\mathrm{B_C}$, (d): $11\mathrm{B_C}$, (e): $1\mathrm{B_C}$, (f): $1\mathrm{B_C}$, where $\mathrm{B_C}$ is the C-band's width.

V. Considering Modal Overlap

From the results in Section IV, one could conclude that 3-FWM gives almost equal results as 1-FWM or 2-FWM in the considered parameter ranges. However, the power of a generated FWM idler also depends on the nonlinearity coefficient. For this feasibility study, we approximate the idler power as [9]

$$\mathrm{P_I} = 4(\gamma^{\mathrm{A,B,C,D}})^2\,\mathrm{L}^2\,\mathrm{P_{P_1}}\,\mathrm{P_S}\,\mathrm{P_{P_2}}\,\mathrm{e}^{-\alpha\,\mathrm{L}}\,|\eta_{\mathrm{FWM}}(\Delta\beta)|^2, \tag{11}$$

with waveguide length L, attenuation α and laser powers $\mathrm{P_{P_1}}$, $\mathrm{P_S}$, $\mathrm{P_{P_2}}$. The nonlinearity coefficient is defined as [9], [12]

$$\gamma^{\mathrm{A,B,C,D}} = \frac{\omega_0\,\mathrm{n_2}}{\mathrm{c_0}\,\mathrm{A}_{\mathrm{eff,cross}}^{\mathrm{A,B,C,D}}} \tag{12}$$

with nonlinear refractive index $\mathrm{n_2}$ and speed of light in vacuum $\mathrm{c_0}$. The cross effective area between involved modes is given by [12]

$$\mathrm{A}_{\mathrm{eff,cross}}^{\mathrm{A,B,C,D}} = \frac{\sqrt{\mathcal{I}^{\mathrm{A}}\mathcal{I}^{\mathrm{B}}\mathcal{I}^{\mathrm{C}}\mathcal{I}^{\mathrm{D}}}}{\left|\iint\left[\left(\vec{F}^{\mathrm{A}}\right)^*\cdot\vec{F}^{\mathrm{B}}\right]\left[\left(\vec{F}^{\mathrm{C}}\right)^*\cdot\vec{F}^{\mathrm{D}}\right]\mathrm{dA}\right|}, \tag{13}$$

where $\vec{F}^{\mathrm{X}}$ are the transversal mode profiles, $(.)^*$ denotes complex conjugation, $\mathcal{I}^{\mathrm{X}} = \iint\left|\vec{F}^{\mathrm{X}}\right|^2\mathrm{dA}$ and integrals are taken over the waveguide cross section.

We can fix ω_0 in Eq. (12) to the same value for all optimizations, since it scales all results equally. We selected the highest simulated frequency, i.e., the lowest wavelength of the O-band. Since we are only interested in the approximate difference in idler powers between different geometries, we can safely neglect that the mode profiles in the integrals in Eq. (13) change with pump and signal frequencies. Furthermore, for these integrals, we only consider regions *inside* of the waveguide core. This way, we avoid integrating over material borders where the electrical field shows Dirac-delta-like behavior. Integrating over borders needs a much higher resolution and even then the results are distorted. Finally, note that although the idler power depends on waveguide length, the nonlinearity parameter does not. Despite having performed FMF PM with the artificially short $\mathrm{L} = 10\,\mathrm{m}$, we use a

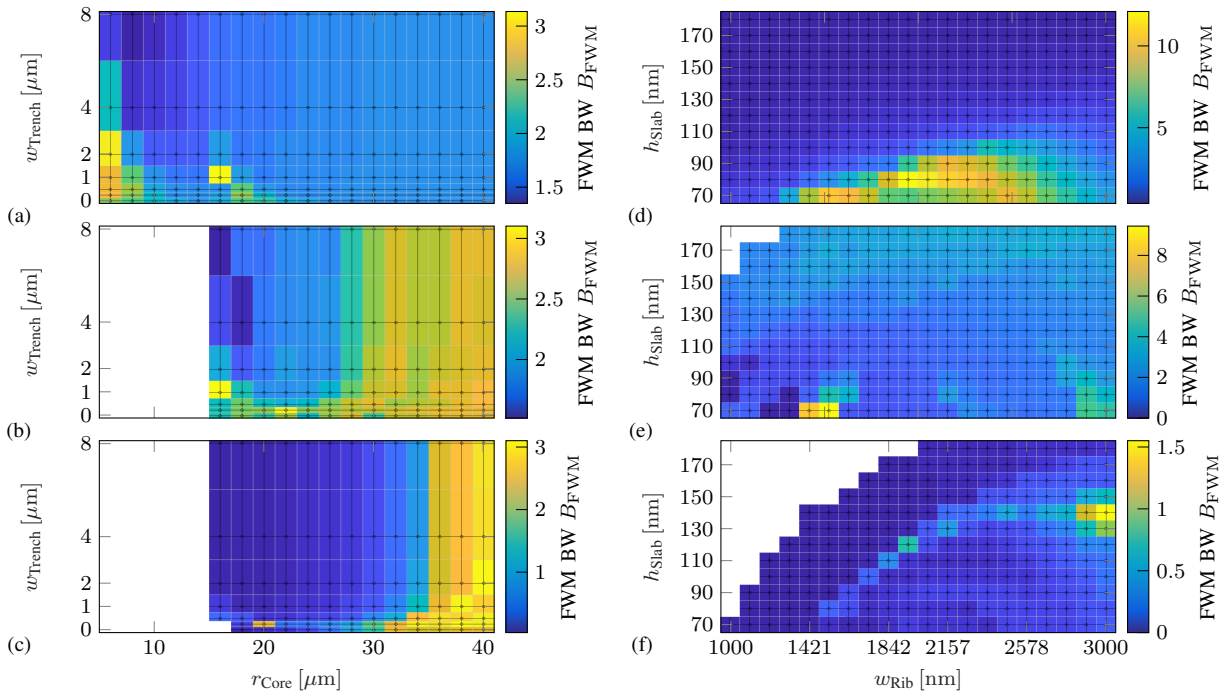

Fig. 7. Highest achievable FWM bandwidths for FMFs and NR waveguides with different geometries. All normalized to multiples of the C-band's frequency range. Waveguides in white areas don't support enough guided modes. (a) 1-FWM in FMFs. (b) 2-FWM in FMFs. (c) 3-FWM in FMFs. (d) 1-FWM in NR waveguides. (e) 2-FWM in NR waveguides. (f) 3-FWM in NR waveguides.

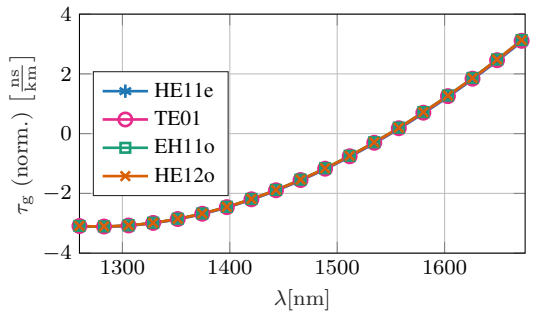

Fig. 8. Relative normalized group delay of modes in a FMF with $r_{\text{Core}} = 40\,\mu\text{m}$, $w_{\text{Trench}} = 0\,\mu\text{m}$ and $r_{\text{Clad}} = 50\,\mu\text{m}$.

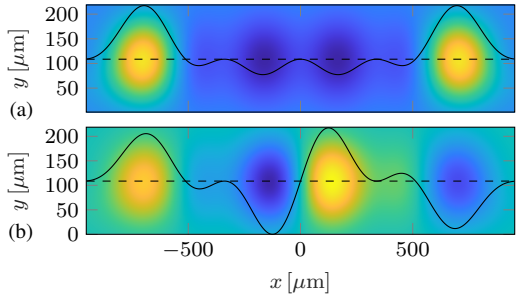

Fig. 9. Examples of overlapped NR waveguide ($w_{\text{Rib}} = 1947\,\text{nm}$ and $h_{\text{slab}} = 80\,\text{nm}$) mode fields A, B, C, and D for two configurations. The fields are scaled for the plots and magnitude units are irrelevant here.
(a): Acceptable nonlinear interaction with $\text{TE}_3, \text{TE}_1, \text{TE}_2, \text{TE}_2$.
(b): Poor nonlinear interaction with $\text{TE}_3, \text{TE}_0, \text{TE}_2, \text{TE}_2$.

realistic fiber length of 4.7 km for computing the idler power in Eq. (11).

Figure 9 shows two configurations of overlapped and multiplied fields (i.e., the integrand in the denominator of $A_{\text{eff,cross}}^{\text{A,B,C,D}}$ in Eq. (13)) of an exemplary NR waveguide. The black lines show field magnitudes over the horizontal dimension. It can be seen that the integral over Fig. 9(a) will give a positive number and the integral over Fig. 9(b) will be close to zero, since positive and negative lobes cancel each other. Therefore, the idler power will be much higher for the first case. Computed nonlinearity coefficients in the example are 20.2/(W m) and 0.0058/(W m) – a factor of more than 35 dB.

In the following, we present FWM bandwidths and nonlinearity coefficients, but force the optimizer to only accept FWM configurations where nonlinearity coefficients have at least a predefined minimal value. For FMFs, this value is $\gamma >= 1{\cdot}10^{-4}/(\text{W m})$ and for NR waveguides $\gamma >= 30/(\text{W m})$. We selected these numbers, since they represent roughly 10% of the highest achievable values in their respective waveguide types.

Few-Mode Fibers: Firstly, enforcing γ values above the chosen threshold does not change the results for 1-FWM, meaning that all configurations in Fig. 7(a) have γ values above the threshold. Secondly, comparing Fig. 10(a) with Fig. 7(b) shows that enforcing a minimal γ also does not have a huge effect on 2-FWM. We see similar bandwidths, except for fibers with $r_{\text{core}} = 40\,\mu\text{m}$. Note, however, that the configurations (wavelengths and mode choices) which lead to the values in Fig. 10 can differ from those leading to Fig. 7, since they are the result of a completely new optimization. A bandwidth of zero in the figure means that our limit on γ could not be achieved by any FWM configuration. The reason

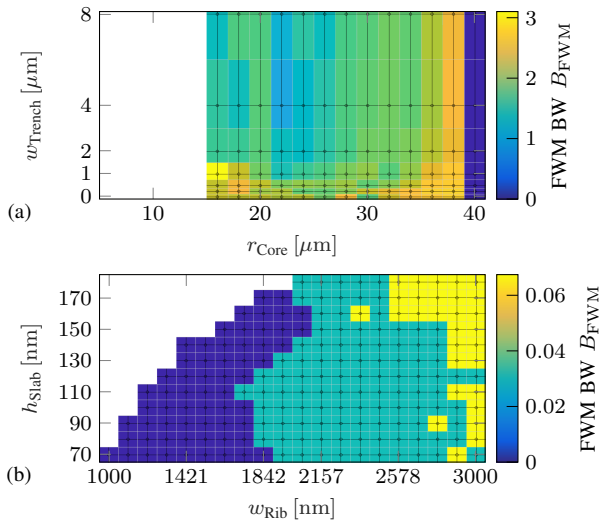

Fig. 10. FWM bandwidths for FMFs and NR waveguides with enforced high nonlinearity coefficients. Bandwidths are normalized to multiples of the C-band's frequency range. Waveguides in white areas don't support enough guided modes.
(a): 2-FWM in FMFs under the constraint $\gamma >= 1 \cdot 10^{-4}/(\mathrm{W\,m})$.
(b): 3-FWM in NR waveguides under the constraint $\gamma >= 30/(\mathrm{W\,m})$.
The figures for 1-FWM in FMFs, 1-FWM in NR waveguides, and 2-FWM in NR waveguides are exactly the same as Fig. 7(a), Fig. 7(d) and Fig. 7(e), respectively, and are not repeated here. The bandwidths for 3-FWM in FMFs are always zero (γ too small) and hence we don't include a figure.

is that larger cores have larger effective areas, which leads to lower nonlinearity (see Eq. (12)). For OPC, the maximal bandwidth is still 1.8, as in Fig. 7. Finally, there is no 3-FWM configuration in the FMFs considered here with γ values above our limit. Therefore, idler powers are very weak and we consider 3-FWM in FMFs as infeasible.

Figure 11(a) shows the resulting nonlinearity coefficients γ for the constrained optimization (Fig. 10). It is clear that larger cores have lower nonlinearity and that almost all waveguides have γ values at least 5 times higher than our limit. Figure 11(a) and Fig. 7(a) reveal that waveguides with small cores have high 1-FWM bandwidth and high nonlinearity coefficients. For 2-FWM, Fig. 11(b) shows that γ values are lower (roughly around our limit) and the good PM configurations for large cores in Fig. 7(b) have low nonlinearity. However, the configurations with core sizes around 16 µm have good bandwidth, acceptable nonlinearity coefficients and 2-FWM is feasible in those fibers.

Nano-Rib Waveguides: Enforcing γ values above the chosen threshold does not change the bandwidths in 1-FWM and 2-FWM. Comparing Fig. 10(b) with Fig. 7(f) shows that 3-FWM is severely affected by enforcing high γ values. But, in contrast to FMFs, NR waveguides *do* support 3-FWM. However, the bandwidth is reduced by orders of magnitude to roughly 250 GHz, which still can be enough for processing a few optical channels. For OPC, the maximum bandwidth is slightly higher at 0.16.

Figure 11 (c) and (d) show that almost all NR geometries support FWM configurations with high γ values. For 1-FWM, all configurations have nonlinearity coefficients above 100/(W m). For 2-FWM, the coefficients are close to

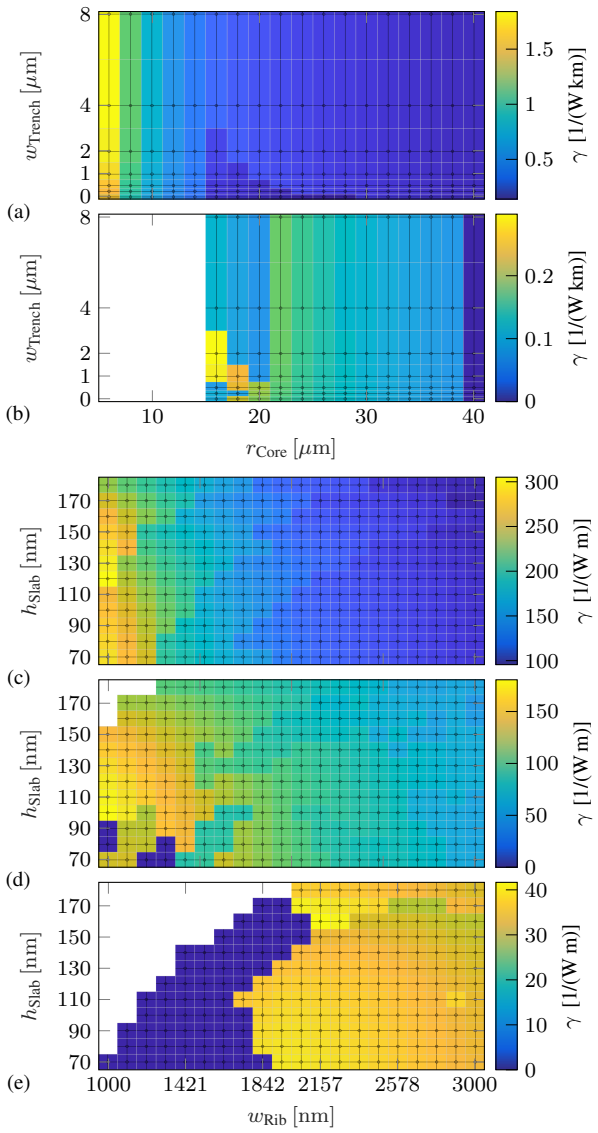

Fig. 11. Approximate nonlinearity coefficients for the same configurations as in Fig. 10 (Fig. 7 for subfigures which are not repeated in Fig. 10). Waveguides in white areas don't support enough guided modes.
(a): 1-FWM in FMFs. (b): 2-FWM in FMFs. (c): 1-FWM in NR waveguides. (d): 2-FWM in NR waveguides. (e): 3-FWM in NR waveguides. We don't include a figure for 3-FWM in FMFs, since the threshold $\gamma >= 1 \cdot 10^{-4}/(\mathrm{W\,m})$ is never fulfilled.

100/(W m) (220 in OPC), except for some scattered geometries where PM fails. To understand the reason for this failure, Fig. 12 shows dispersion curves of one of those waveguides. The group delay curves do not have any vertical overlap, which means 2-FWM is impossible (see Eq. (6)).

Finally, Fig. 11(e), shows that NR 3-FWM γ values are not very sensitive to geometry variations and the coefficients are around 40/(W m) (60 in OPC).

VI. Idler Power Evolution

The results in sections Sections IV and V are based on the FWM efficiency η_{FWM} Eq. (10). This metric relies on three main approximations: 1) The attenuation is constant (neither frequency, nor mode dependent). 2) There is no

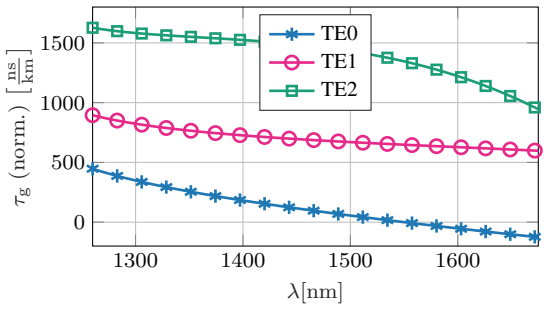

Fig. 12. Relative normalized group delay of modes in a NR waveguide with $w_{\text{Rib}} = 1210.53\,\text{nm}$ and $h_{\text{Slab}} = 70\,\text{nm}$.

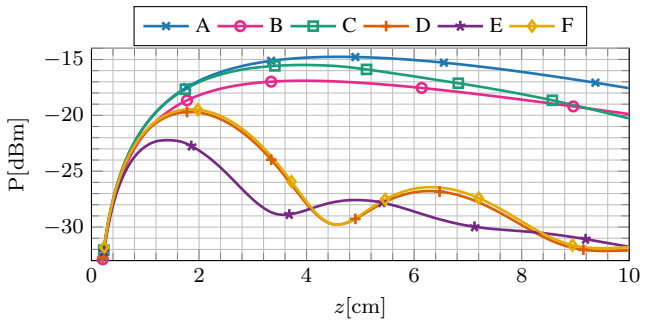

Fig. 13. Simulated evolution of the BS idler in the NR waveguide with rib width 3000 nm and slab height 140 nm, with five different propagation settings. See main text for settings values.

linear coupling. 3) The pumps and signal are not depleted by the nonlinear interaction. The third assumption is usually fulfilled in all-optical signal processing experiments, since the pumps and signal are much stronger (usually around 20 dBm and 10 dBm) than the generated idler (typically less than −20 dBm). However, due to the first two assumptions, η_{FWM} fails to capture variable attenuation and linear coupling, which usually need to be considered in real-world applications. The FWM efficiency can be remarkably exact, though, when linear coupling is low due to few propagating modes and the attenuation is flat due to small considered wavelength differences, e.g. in [9] or [2].

In many of our presented configurations, attenuation is quite likely frequency dependent due to the large considered bandwidths. Also, the waveguides we consider potentially allow the propagation of many guided modes, especially those with large cores. Since the group delays of neighboring modes are very close in these waveguides (see e.g. Fig. 8), linear coupling will also have an effect on FWM. Nevertheless, η_{FWM} serves as a good metric for a best-case analysis – given that modal overlap is considered as well (as in Section V). For example, FWM efficiency predicted the bandwidth quite well in our NR waveguide-based all-optical C- to O-band wavelength conversion experiment [4]. However, linear crosstalk was much more severe in previous NR waveguide generations we had manufactured, prohibiting efficient conversion.

The interplay of variable attenuation, linear coupling and phase mismatch can lead to quite different nonlinear behavior (see e.g. [10] or [13, Ch. 3]). As an example, the idler evolution in an exemplary waveguide ($w_{\text{Rib}} = 3000\,\text{nm}$ and $h_{\text{Slab}} = 140\,\text{nm}$) is shown in Fig. 13 under different assumptions A to F. The power was computed with a frequency domain continuous wave simulation including attenuation, linear coupling (considering modes TE_0 to TE_3) and nonlinear coupling (based on Eq. (1) in [14]). Here we used a constant nonlinear susceptibility $\chi^{[3]} = (3.77 - 0.224j) \cdot 10^{-19}\,\text{V}^2/\text{m}^2$ or, equivalently, $n_2 = 10 \cdot 10^{-18}\,\text{m}^2/\text{W}$ and $\beta_{\text{TPA}} = 0.5 \cdot 10^{-11}\,\text{m/W}$. The figure shows BS idlers in a 3-FWM configuration where the signal was launched into mode TE_2 at wavelength 1502.0 nm with power 10 dBm, pump 1 into TE_2 at 1316.0 nm with 20 dBm, pump 2 into TE_3 at 1263.9 nm with 20 dBm and the idler evolved in TE_1 at 1576.1 nm. These wavelengths and modes are the optimum which lead to the bandwidth shown in Fig. 10 for $w_{\text{Rib}} = 3000\,\text{nm}$ and $h_{\text{Slab}} = 140\,\text{nm}$.

In scenario A, we assumed a flat attenuation of 1 dB/cm, no linear coupling and perfect PM. In B, we changed to mode- and frequency dependent loss – ranging from 0.56 dB/cm to 2.6 dB/cm, increasing with frequency and mode order. In C, we added linear coupling which couples all modes. Linear coupling is caused by random fluctuations of waveguide imperfections and we selected a model which leads to a pump crosstalk similar to [4]. Therefore, crosstalk in a real waveguide can be both, higher or lower than our selected value here. In D, we moved the signal frequency from it's optimum to the border of the PM region, which created a phase mismatch of $\Delta\beta = 140/\text{m}$. The border was defined in Definition 1 such that the idler should drop by 3 dB at the waveguide's end (2 cm). As one can see in the figure, the difference between A and D is indeed close to 3 dBm at 2 cm. Scenario E combines variable attenuation, linear coupling and phase mismatch and one can see that it's behavior is different. Finally, scenario F is like D, but the two photon absorption coefficient was set to $\beta_{\text{TPA}} = 0$ – the effect is very small.

A waveguide length of 2 cm is not the optimum for this waveguide in terms of generated idler power. However, our goal was to optimize and compare FWM bandwidths among different waveguide geometries and FWM types and hence we fixed the waveguide lengths – allowing for a fair comparison.

VII. Conclusions

We showed that 1-FWM and 2-FWM perform better than 3-FWM in both, FMFs and NR waveguides. FWM bandwidths as well as approximative nonlinearity coefficients are both larger. 3-FWM is achievable in some NR waveguides with acceptable efficiency in narrowband operation. Depending on the intended use case, it might be acceptable to sacrifice some idler power and broadband operation to gain the flexibility to place signal, pump and idler in three different modes. 4-FWM does not work in neither FMFs, nor in NR waveguides. Our results are a best-case analysis of phase matching and actual FWM bandwidth can be smaller than the presented values.

References

[1] K. O. Hill, D. C. Johnson, B. S. Kawasaki, and R. I. MacDonald, "CW three-wave mixing in single-mode optical fibers," *J. Appl. Phys.*, vol. 49, pp. 5098–5106, 1978.

[2] R.-J. Essiambre, M. A. Mestre, R. Ryf, A. H. Gnauck, R. W. Tkach, A. R. Chraplyvy, Y. Sun, X. Jiang, and R. Lingle, "Experimental investigation of inter-modal four-wave mixing in few-mode fibers," *IEEE Photon. Technol. Lett.*, vol. 25, pp. 539–542, 2013.

[3] C. Koos, L. Jacome, C. Poulton, J. Leuthold, and W. Freude, "Nonlinear silicon-on-insulator waveguides for all-optical signal processing," *Opt. Express*, vol. 15, p. 5976, 2007.

[4] G. Ronniger, I. Sackey, T. Kernetzky, U. Höfler, C. Mai, C. Schubert, N. Hanik, L. Zimmermann, R. Freund, and K. Petermann, "Efficient ultra-broadband C-to-O band converter based on multi-mode silicon-on-insulator waveguides," in *2021 European Conference on Optical Communication (ECOC)*. Bordeaux, France: IEEE, 2021, pp. 1–4.

[5] T. Kernetzky, G. Ronniger, U. Höfler, L. Zimmermann, and N. Hanik, "Numerical optimization and CW measurements of SOI waveguides for ultra-broadband C-to-O-band conversion," in *2021 European Conference on Optical Communication (ECOC)*. Bordeaux, France: IEEE, 2021, pp. 1–4.

[6] T. Kernetzky, Y. Jia, and N. Hanik, "Multi dimensional optimization of phase matching in multimode silicon nano-rib waveguides," in *Photonic Networks; 21st ITG-Symposium*, Leipzig, Germany, 2020, p. 8.

[7] R. Maruyama, N. Kuwaki, S. Matsuo, and M. Ohashi, "Two mode optical fibers with low and flattened differential modal delay suitable for WDM-MIMO combined system," *Opt. Express*, vol. 22, p. 14311, 2014.

[8] A. B. Fallahkhair, K. S. Li, and T. E. Murphy, "Vector finite difference modesolver for anisotropic dielectric waveguides," *J. Lightw. Technol.*, vol. 26, pp. 1423–1431, 2008.

[9] G. Rademacher, R. S. Luis, B. J. Puttnam, H. Furukawa, R. Maruyama, K. Aikawa, Y. Awaji, and N. Wada, "Investigation of intermodal four-wave mixing for nonlinear signal processing in few-mode fibers," *IEEE Photon. Technol. Lett.*, vol. 30, pp. 1527–1530, 2018.

[10] Y. Xiao, R.-J. Essiambre, M. Desgroseilliers, A. M. Tulino, R. Ryf, S. Mumtaz, and G. P. Agrawal, "Theory of intermodal four-wave mixing with random linear mode coupling in few-mode fibers," *Opt. Express*, vol. 22, p. 32039, 2014.

[11] M. Borghi, C. Castellan, S. Signorini, A. Trenti, and L. Pavesi, "Nonlinear silicon photonics," *J. Opt.*, vol. 19, p. 093002, 2017.

[12] G. Rademacher and K. Petermann, "Nonlinear gaussian noise model for multimode fibers with space-division multiplexing," *J. Lightw. Technol.*, vol. 34, pp. 2280–2287, 2016.

[13] M. E. Marhic, *Fiber Optical Parametric Amplifiers, Oscillators and Related Devices*. Cambridge: Cambridge University Press, 2007.

[14] U. Höfler, T. Kernetzky, and N. Hanik, "Modeling material susceptibility in silicon for four-wave mixing based nonlinear optics," in *2021 International Conference on Numerical Simulation of Optoelectronic Devices (NUSOD)*. Turin, Italy: IEEE, 2021, pp. 121–122.